Evaluation of Anisotropic Conductive Films Based on Vertical Fibers for Post-CMOS Wafer-Level Packaging

Mamadou Diobet Diop, *Member, IEEE*, Moufid Radji, *Senior Member, IEEE*, Anas A. Hamoui, Yves Blaquière, *Member, IEEE*, and Ricardo Izquierdo, *Member, IEEE*

***Abstract*— In this paper, we investigate the mechanical and electrical properties of an anisotropic conductive film (ACF) on the basis of high-density vertical fibers for a wafer-level packaging (WLP) application. As part of the WaferBoard, a reconfigurable circuit platform for rapid system prototyping, ACF is used as an intermediate film providing compliant and vertical electrical connection between chip contacts and a top surface of an active wafer-size large-area IC. The chosen ACF is first tested by an indentation technique. The results show that the elastic–plastic deformation mode as well as the Young's modulus and the hardness depend on the indentation depth. Second, the efficiency of the electrical contact is tested using a uniaxial compression on a stack comprising a dummy ball grid array (BGA) board, an ACF, and a thin Al film. For three bump diameters, as the compression increases, the resistance values decrease before reaching low and stable values. Despite the BGA solder bumps exhibit plastic deformation after compression, no damage is found on the ACF film. These results show that vertical fiber ACFs can be used for nonpermanent bonding in a WLP application.**

***Index Terms*— Anisotropic conductive film, contact resistance, elastic-plastic deformation, wafer-level packaging.**

I. Introduction

ANISOTROPIC conductive films (ACFs) continue to gain popularity in the assembly of electronic devices. ACFs are electrically conductive in the z-axis direction (z-axis film), but highly insulating in the horizontal plane. They are used as an interconnect material in packaging technologies, such as chip-on-glass (COG), chip-on-flex (COF), chip-on-board (COB), flex-on-board (FOB) and flex-on-glass (FOG). A single z-axis film can replace a whole array of solder joints, thereby greatly reducing the processing cost; moreover, ACFs do not contain lead and require no flux, thus making them an environmentally friendly alternative to solder; and ACFs do not require the underfill step necessary in solder bumping for flip-chip assembly. ACFs also enable fine pitch applications [1]–[4].

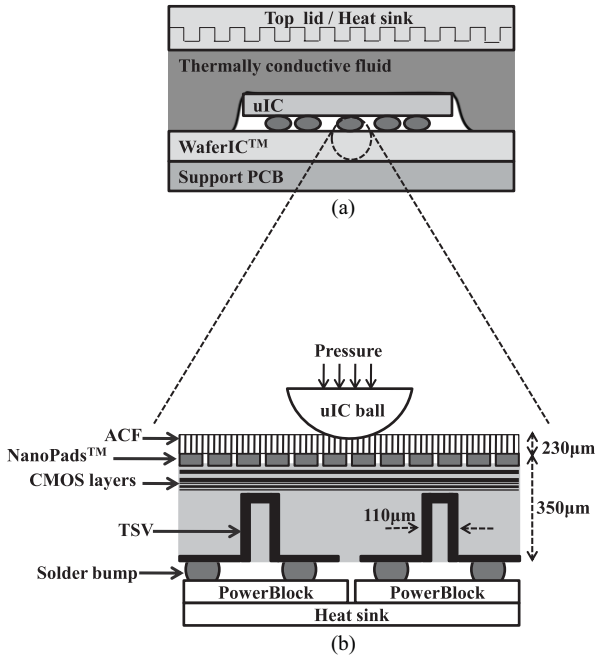

Fig. 1. WaferBoard system. (a) WaferBoard cross-section. (b) WaferIC assembly cross-section.

However, ACFs need specific application and characterization in order to extend their use. Here, ACF evaluation is done as part of the development of WaferBoard, a reconfigurable wafer-scale circuit platform for rapid prototyping of electronic systems.

A detailed description of the WaferBoard platform can be found in [5]. The WaferBoard concept is illustrated in Fig. 1(a). The top of the platform is a mechanical lid that integrates a heat sink and a pouch filled with a thermally conductive fluid. The role of the mechanical lid is to apply mechanical pressure onto the conventional chips or user ICs (uICs) with the pouch while carrying heat from the uICs' tops to the outside environment. The uIC is placed on the main component of the WaferBoard platform which is an active wafer-size large-area IC (LAIC) named WaferIC. The WaferIC is used to programmably interconnect any uICs on its surface. The WaferIC is attached to a support PCB.

Manuscript received September 26, 2011; revised November 10, 2012; accepted January 10, 2013. This work was supported in part by the Gestion TechnoCap Inc. and DreamWafer Division, Mitacs, the Fond Québecois de la Recherche Sur la Nature et les Technologies, the Natural Sciences and Engineering Research Council of Canada, Prompt Quebec, and the CMC Microsystems. Recommended for publication by Associate Editor R. V. Tanikella upon evaluation of reviewers' comments.

M. D. Diop, Y. Blaquière, and R. Izquierdo are with the Département d'informatique de l'Université du Québec à Montréal, Montréal, QC H2X 3Y7, Canada (e-mail: diopdiobet@gmail.com; blaquiere.yves@uqam.ca; izquierdo.ricardo@uqam.ca).

M. Radji and A. A. Hamoui are with the Department of Electrical and Computer Engineering, Mc-Gill University, Montreal, QC H3A 2A7, Canada (e-mail: moufid.radji@gs.com; anas.hamoui@mcgill.ca).

Color versions of one or more of the figures in this paper are available online at http://ieeexplore.ieee.org.

Digital Object Identifier 10.1109/TCPMT.2013.2243203

During the prototyping operation, the uICs are manually placed on top of the WaferIC, without concern for alignment. The lid is closed to press the uICs closely on to the wafer top surface. The WaferIC senses the component contacts and recognizes uIC packages and intelligently interconnects the contacts according to the user netlist. The electronic system prototype is then ready to be brought up and run, and all system functionalities can be validated. The uIC packages can be of any surface mount type with horizontal or flat pads such as quad flat packages (QFPs) and thin small outline packages (TSOPs), or ball grid array (BGA) packages.

The cross-sectional view of the WaferIC assembly is presented in Fig. 1(b). This assembly is composed of four main stacked layers corresponding to the ACF film, the 8-inch wafer itself, the PowerBlocks, and the heat sink base. The ACF is placed on top of the wafer as an intermediate layer between uICs' contact pads (ball for BGA package) and the top structures of the WaferIC, which consists of more than one million tiny (e.g., 80 $\times$80 μm) conducting pads called NanoPads that are connected through a reconfigurable network. The WaferIC also contains through silicon vias (TSVs) that connect the backside power regulator to the first metal layer M1, which will relay the power and ground connections to the upper CMOS layers. TSVs also provide Joint Test Action Group signals to configure the WaferIC internal circuitry prior to operation. The electrical characterization of TSVs at wafer level used for this application was done in [6]. PowerBlocks are attached to the backside wafer by a flip-chip process and are constituted of an array of miniature PCBs that integrate regulators to supply dc power to the backside wafer. This structure stands on a solid heat sink that dissipates heat from both the backside of the WaferIC and PowerBlocks. They supply 3.3 and 1.8 V to the wafer.

The ACF is required to provide sufficient ductility and deformability allowing uIC contacts to be pressed into it to the extent needed to make good electrical connections to the NanoPads on the other side. The film must also offer good thermal conductivity to ensure heat dissipation throughout the structure. Two additional requirements for the ACF dictated by the application are the necessity for a wafer-size film which covers the entire 8-inch WaferIC and the possibility to use the film without a bonding or lamination step as ACF placement occurs toward the end of the WaferIC assembly. While most of previous studies were focused on spherical ACF particles with permanent bonding applications [1]–[4], here we present the use of vertical ACF structures without using a bonding process. In addition, our paper is done in the context of wafer-level packaging (WLP) solutions.

Section II covers some theoretical predictions of ACFs, the determination of the optimal ACF for the WLP application, and the presentation of the electrical and mechanical setup. In Section III, we present the mechanical evaluation of the ACF using the indentation technique. The purpose is to understand the mechanical behavior of the film in uniaxial compression testing as well as to extract its mechanical properties. Section IV reports the electrical and mechanical evaluation of the contact between a dummy BGA package and ACFs which are of high interest to WLP applications.

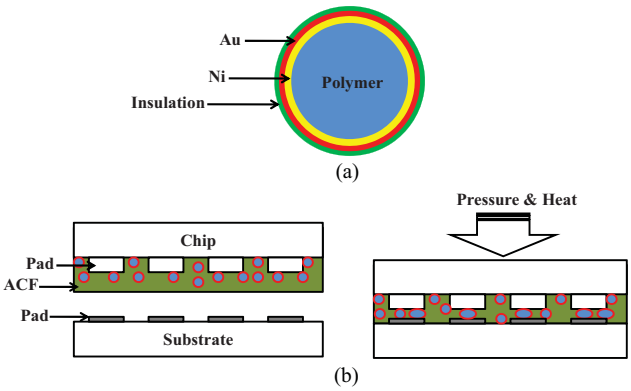

Fig. 2. Spherical ACF. (a) Particle structure. (b) Bonding process. Conductive particles are trapped between corresponding pads of IC and substrate; protective polymer is removed in areas where pressure and heat are applied allowing for vertical conduction through Ni–Au layer; particles are maintained in compressed state after epoxy curing, improving electrical contact [2].

II. Material and Experiment

A. Spherical Particle ACF Versus Vertical Fiber ACF

There are various types of ACF with different particle shape and composition and different polymer matrices. The most common ACF is made of spherical polymer particles plated with nickel–gold and is protected from neighboring particles by an additional insulating layer. The conductive sphere, which can be filled or hollow, is shown in Fig. 2(a) and the ACF bonding process is presented in Fig. 2(b). ACF solutions can be laminated on an entire silicon substrate as a part of a flip-chip assembly for WLP application [2]. Some of the drawbacks of using spherical particle ACFs are the possibility of lateral shorting of adjacent pads and vertical opening between facing pads [3]. A tradeoff must be made between a good vertical conduction requiring a high particle density and a good xy plane insulation achieved with lower particle density. Moisture absorption has also been reported as a reliability issue for spherical particle ACFs. This moisture tends to induce mechanical failures at the interface between the chip and the ACF or between the substrate and the ACF [4], [7].

Another more recent type of ACF film substitutes the conductive sphere with continuous vertical fibers. This type of film can achieve ultrahigh-density connections. Unlike spherical particles, vertical metal fibers are inherently anisotropic, thereby limiting the chances of lateral shorting. Using V_m and V_f, the volumetric factors of the matrix and the fibers, respectively, one can approximate the isotropic Young's modulus for spherical particles as [8]

$$E \approx \frac{9KG}{3K+G} \tag{1}$$

where

$$K \approx \frac{E_m}{3\,(1-2\upsilon\vartheta_m)}\left\{1+3\left(\frac{1-\vartheta_m}{1+\vartheta_m}\right)\frac{V_f}{1-Vf}\right\} \tag{2}$$

$$G \approx \frac{E_m}{2\,(1+\vartheta_m)}\left\{1+\frac{15}{2}\left(\frac{1-\vartheta_m}{4-5\vartheta_m}\right)\frac{V_f}{1-Vf}\right\} \quad (3)$$

$$\vartheta_m = \left(\frac{3K-2G}{3K+G}\right). \quad (4)$$

For vertical fibers, the only modulus component which matters is the longitudinal modulus of the film E_l. Assuming E_m and E_f are the Young's modulus of the matrix and the fibers, respectively, the longitudinal modulus E_l of the ACF is defined by using the rule of mixture as follows [8]:

$$E_l = E_f V_f + E_m V_m \quad (5)$$

if the ACF is void free

$$V_f + V_m = 1 \quad (6)$$

by inserting (6) into (5) gives

$$E_l = E_f V_f + E_m\left(1-V_f\right). \quad (7)$$

In practice, the modulus of the matrix is negligible compared with the modulus of the fiber ($E_m \ll E_f$) thus, the longitudinal modulus of the ACF based on vertical fibers depends essentially on the fiber Young's modulus E_f [see in (7)] whereas in (1) to (4) the spherical particle ACF's modulus depends on the modulus of the matrix E_m.

From a mechanical point of view, in 3-D stacking, pressure is applied on the ACF along the vertical direction by compression or tensile loading; thus, by using vertical fiber ACFs, the fibers support the load, giving high tensile-compression strength. On the contrary, when the ACF is made with spherical particles, only the matrix supports the load, giving rise to low tensile-compression strength. On the WLP application presented here, significant vertical pressures are expected to be applied to achieve a proper electrical and mechanical contact. It is crucial that the chosen ACF withstands this pressure while remaining elastic. The high tensile compression strength of vertical fiber ACFs are therefore preferred. Besides, vertical fiber ACF has higher vertical thermal conductivity compared to spherical particle ACF due to the continuous and aligned fibers. Based on the aforementioned qualitative factors, only vertical fiber ACFs are investigated from here on. Table I is a qualitative comparison of some properties for both ACF film types for WaferBoard application.

B. Micromechanics of ACF-Based Vertical Fibers

Here, the effects of microstructures, such as the fiber misalignment, the contiguity in the vertical direction, and the elastic buckling are briefly explored.

Equation (7) assumes that the fibers are parallel and regularly embedded in a homogeneous matrix ignoring the fiber misalignment and contiguity. Instead, the fibers are often spaced with a certain dispersion where some are touching each other; alignment imperfections are also common where fibers are not perfectly straight. So, the theoretical models must be modified to account for more realistic ACFs. Tsai [9] proposed models in which the misalignment and contiguity effects were considered. The misalignment factor was incorporated in the prediction of the longitudinal modulus E_l by multiplying (7) by the fiber misalignment factor k. The factor k varies from 0.9 to 1.

TABLE I
QUALITATIVE COMPARISON BETWEEN SPHERICAL AND VERTICAL ACFS FOR WAFERBOARD APPLICATION

Characteristics	Spherical ACF	Vertical ACF
Risk of lateral electrical short between adjacent pads	Yes (particle accumulation)	No
Risk of vertical electrical open between facing pads	Yes (lower particle density)	Low
Tensile/compression strength	Lower	Higher
Vertical thermal conductivity	Lower	Higher

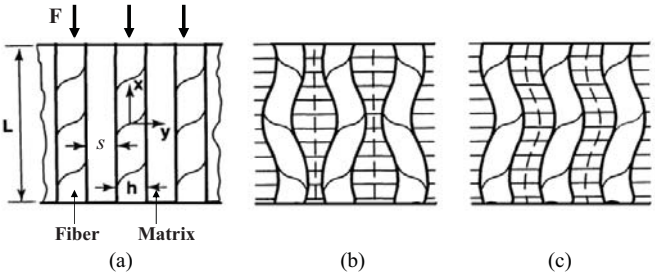

Fig. 3. Composite buckling model proposed by Rosen [10]. (a) Representative volume element. (b) Extension mode. (c) Shear mode.

The contiguity factor C varies between 0 and 1; $C = 0$ corresponds to no contiguity (fibers are isolated) and $C = 1$ represents a perfect contiguity (fibers are in contact). In Tsai's theory, the contiguity factor was only considered in the theoretical prediction of the transversal modulus, the shear modulus, and the transverse Poisson's ratio. These properties are ignored in this paper where only the uniaxial stresses in the vertical direction are considered. Depending on the study, the factors k and C can be determined by comparing the theoretical models with the experimental results [10].

The fiber buckling under compressive stress is interesting to study since the ACF is under compression during the WaferBoard prototyping. The buckling of the vertical fibers of a composite material can be studied using the theory proposed by Rosen [11]. Using a 2-D model in Fig. 3(a), Rosen assumed that a composite material under compressive stress can experience one of two distinct buckling modes called the extension mode and the shear mode. In the extension mode, as seen in Fig. 3(b), the fibers buckle out of phase relative to one another. Thus, along the fibers, the matrix extends or contracts in y-direction. In the shear mode, the fibers buckle in phase as seen in Fig. 3(c). So, the matrix shears in the xy plane with the entire shear being relative to the x-axis. The compressive strength of the fibers for the extension mode $(\sigma_{fcr})_{\text{extension}}$ is given by

$$(\sigma_{f_{cr}})_{\text{extension}} = 2\sqrt{\frac{V_f E_m E_f}{3(1-V_f)}}. \quad (8)$$

The compressive strength of the fibers for the shear mode $(\sigma_{fcr})_{\text{shear}}$ is given by

$$(\sigma_{f_{cr}})_{\text{shear}} = \frac{G_m}{V_f(1-V_f)} \quad (9)$$

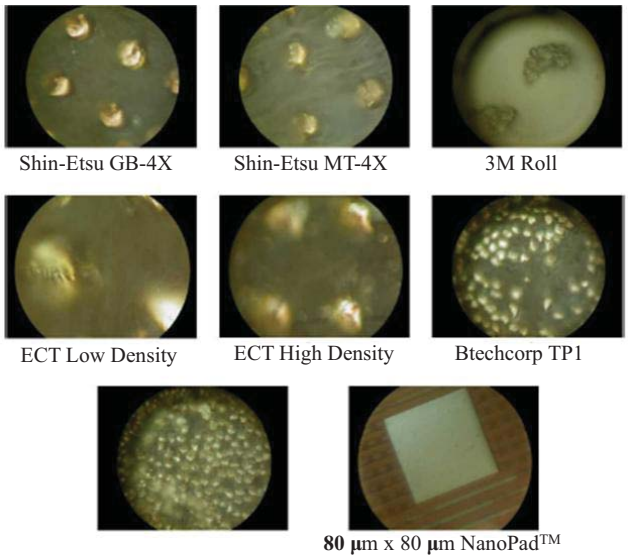

Fig. 4. ACF–NanoPad comparison at matching magnification.

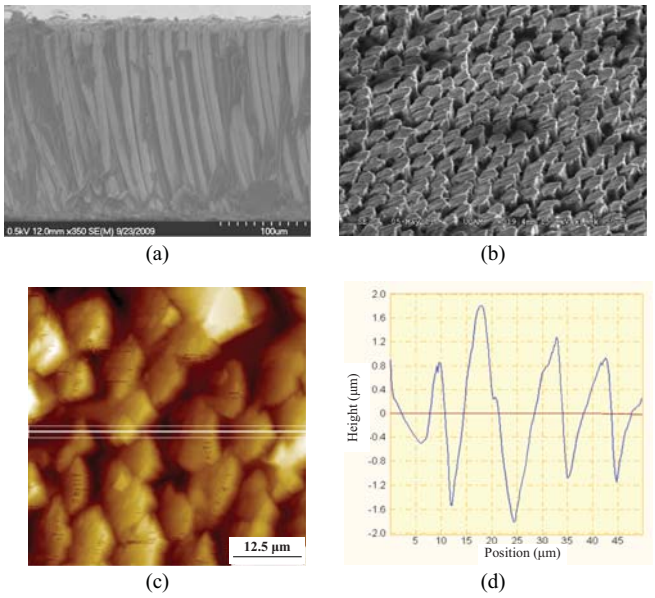

Fig. 5. TP2 micrographs. (a) Cross-sectional view. (b) Top view with 45° tilt. (c) 50 × 50 μm AFM image. (d) Height profile from (c).

where G_m is the matrix shear modulus. The x-direction strain at buckling can be deduced from (8) and (9) and the classical Hooke's stress–strain relationship.

Accordingly, the influence of the fiber spacing s on the compression strength can be predicted through the fiber volume fraction V_f, which is defined by

$$V_f = \frac{h}{h+s}. \tag{10}$$

C. Examination and Selection of ACF-Based Vertical Fibers

Several ACF samples were tested according to various procedures; the ultimate goal is to provide the best electrical contact with the lowest required pressure and in a reproducible fashion. Table II is an overview of the tested films. Preliminary testing, using two probes placed on either side of the film, showed that all samples conduct in the z-direction and exhibit a lateral resistance higher than 40 MΩ when measurement probes are 1 mm apart (negligible lateral conduction). As stated in the Table II, most films are less than 2 cm on a side, except for the Btechcorp and 3M samples. 3M's tape was found to be highly adhesive and not requiring any bonding step. However, due to its low thickness of only 50 μm and its texture, the film provides little elastic deformation under compressive loading. Such properties are desirable in the WaferBoard application, where significant pressure is expected atop the uIC (Fig. 1), which will be transferred to the ACF interfaces. Table III summarizes the measured fiber densities and pitches along with the maximum achievable metal-to-metal contact area on an 80 ×80 μm NanoPad. Btechcorp's TP2 provides the highest density of contact fibers, as can be seen in Fig. 4, and hence the largest contact area. Btechcorp's films were the only ones which could be available in a contiguous 8 × 8 inch sheet, which made them the only choice for the WLP process. In addition to its high density, TP2 also provides a reasonable maximum operating temperature (130 °C), which prevents the polyamide matrix from melting when uIC packages heat up. For instance, some Intel multicore processors have been reported to reach temperatures above 85 °C [12]. Thus, the detailed characterization presented in the next sections is focused on the TP2 film.

D. Characterization of the TP2 ACF Film

The tests were performed with the TP2 film which is a 230-μm-thick composite of cylindrical nickel fibers embedded in a polyamide matrix. The fibers' pitch and their nominal diameter are 11 and 8 μm, respectively. After thermocompression bonding, the TP2 can reach a thermal conductivity of 5 W/(mK). The cross-sectional and the top surface views of the film are seen in Fig. 5(a) and (b), respectively. The fibers have a small tilt of 5° that allows proper consolidation of the polyamide during lamination process. AFM characterization was done allowing extracting the rms roughness Rq of 2.6 μm. Thus, the TP2 surface is very rough over the expected contact area dimension. Fig. 5(c) is one of the 50 × 50 μm height scan images obtained and Fig. 5(d) is the height of some fibers measured by a horizontal line profile. The images in Fig. 5(b) and (d) show the sharp extremity of the Ni fibers and confirm that the top surface of the film is mostly occupied by the fibers rather than the polyamide matrix. However, the whole top surface of the film is not free from defects due to the manufacturing process; some areas contain polyamide residues that partially or totally cover the top surface of the fibers. The contact resistance measurements were impaired when bumps are in contact with such areas. This was solved by choosing ACF coupons free of polyamide residues for the results presented in this paper. Besides, an SEM inspection of the top surface of the fibers of these coupons did not show isolated residues that may influence the establishment of contact resistance.

E. Electrical and Mechanical Test Setup

The TP2 film is required to provide good electrical conductivity between uIC contacts and the wafer top surface

TABLE II
OVERVIEW OF ACF-BASED VERTICAL FIBERS

Company	Sample Name	Approx. Size (cm × cm)	Material Type	Brief Description
Shin-etsu	GB-4X	1.5 × 1.5	Film	500-μm-thick polymer with medium fiber density
	MT-4X	1.5 × 1.5	Film	500-μm-thick medium-density polymer with a 250-μm-thick offset from top to bottom, i.e., fibers at 26°angle
3M	Conductive adhesive 9705	—	Tape	50-μm-thick highly adhesive tape containing large conductive particles
Everett charles technologies	Low density	1 × 1	Film	0.5-mm-thick polymer with coarse fiber distribution
	High density	0.7 × 0.7	Film	1-mm-thick polymer with finer fiber distribution
Btechcorp.	TP1	6 × 6	Film	Around 200-μm-thick very high-density nickel fibers in polyamide
	TP2	6 × 6	Film	Around 200-μm-thick very high-density nickel fibers in polyamide with high bonding temperature than TP1.

TABLE III
COMPARISON OF VARIOUS ACFs WITH 80 × 80 μm NANOPAD

Company		Average Contact Pitch (μm)	Average Diameter (μm)	Contact Number on NanoPad	Contact Area (μm^2)
Shin-etsu	GB-4X	50 × 58	14	2.2	339
	MT-4X	50 × 50	14	2.6	400
3M	Adhesive roll	70 × 70	48	1.3	2352
Everett charles technologies	Low density	106 × 118	35	0.51	491
	High density	63 × 80	14	1.3	200
Btechcorp	TP1	11 × 11	8	14.5	729
	TP2	11 × 11	8	52.9	2659

(NanoPad) without any mechanical damage due to pressure applied on the top of the uIC packages. In order to address this issue, a test bench was designed which comprised of a mechanical press with a pressure plate on a fine control shaft and voltage–current recording instruments. The setup permits simultaneous recording of the applied displacement as well as the resulting electrical contact resistance. This resistance is obtained using a four-point probing technique which partially dissociates the forced current path from the voltage-sensing path, allowing a resistance measurement virtually unaffected by circuit leads and probes. The tests were done by placing the TP2 between a BGA board and a 1-μm-thick Al film deposited on an Si substrate. Fig. 6 shows a schematic of this recording setup. BGAs were chosen over other packages because they are one of the most commonly used package types. Due to practical requirements related to the application of mechanical pressure, in particular, the presence of a topside pressure plate, no commercial BGA packages could be used. Instead, dummy BGA boards with lead-free tin-based solders have been designed and manufactured in-house. Fig. 7(a) shows the photography of a sample dummy BGA board made on a dual-layer FR4 printed circuit board. Clusters of 14 bumps are designed as shown by SEM micrograph in Fig. 7(b), and 8 of these bumps can be probed during contact. Each test bump is connected to 2 pads for four-point measurement; hence each board has 16 pads at its periphery. Vias are created near each of these pads so that probing can be done from either side of the board if needed. Given the large pad size of 3 × 3 mm, long wires to recording instruments can be soldered directly onto the board, without requiring wire bonding to an intermediate circuit.

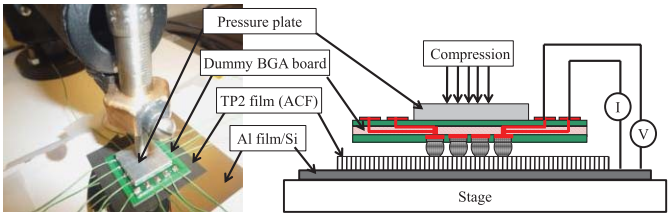

Fig. 6. Electrical and mechanical testing setup.

Before addressing the electrical and mechanical results related to this setup, we present a mechanical study of the TP2 using the indentation technique.

III. MICROINDENTATION RESULTS

The microindentation tests were done using a CSM Micro Combi Tester which continuously controls and monitors the forces and the displacements with a precision of 0.3 mN and 0.3 nm, respectively. Although most indentation studies of composite film use a three-side pyramid tip to separate the properties of the interphase polymer from the fibers [13], [14], we have used a 200-μm-radius spherical diamond indenter in our tests. This particular indenter geometry was chosen

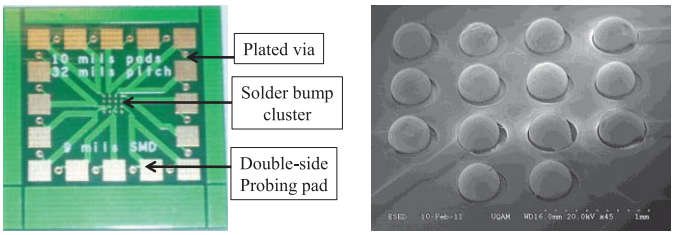

Fig. 7. Dummy BGA board. (a) Photography of the board. (b) SEM micrograph of an array of 370-μm-diameter solder bumps.

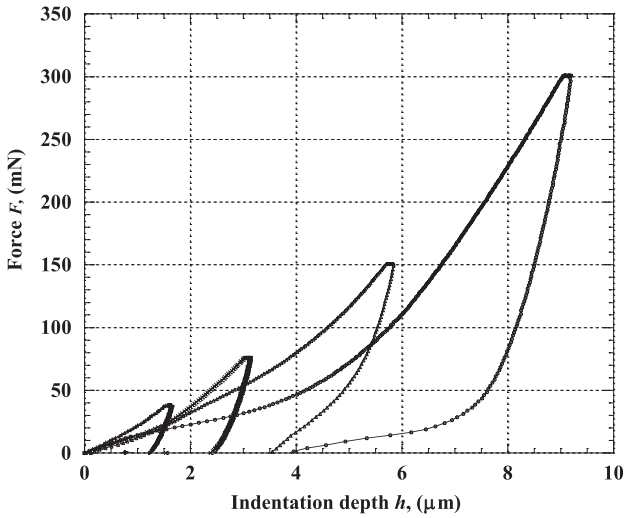

Fig. 8. Force and indentation depth curves at 37.5, 75, 150, and 300 mN.

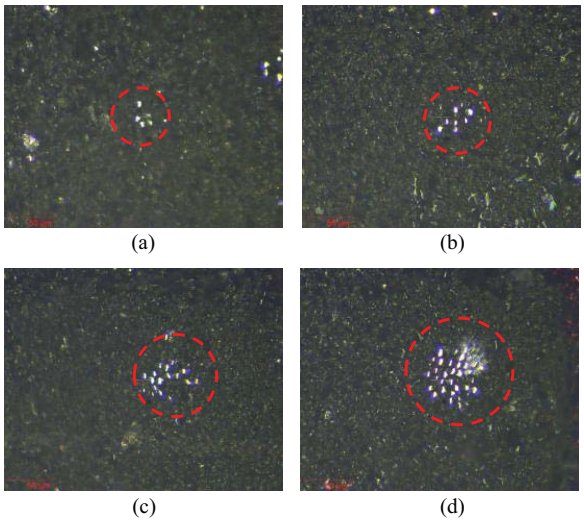

Fig. 9. Residual impression after indentation at (a) 37.5 mN, (b) 75 mN, (c) 150 mN, and (d) 300 mN.

because of its similarity to the geometry of the hemispherical bump contacts of the BGA package and in order to neglect the influence of the film roughness at the contact. Two types of microindentation tests were performed in order to understand the mechanical behavior of the TP2 film as well as to extract modulus E and hardness H as functions of indentation depth. The data presented here are an average of six indentation tests.

A. TP2 Mechanical Behavior

The first type of tests was made in one load–unload cycle at different maximum forces F_m of 37.5, 75, 150, and 300 mN using a constant loading rate of 150 mN/s. Fig. 8 is a plot of the force–depth of the indentation tests. From these curves, we can extract the total indentation work W_{tot} as the area under the loading curve and the energy relaxed during the elastic recovery W_{el} as the area beneath the unloading curve. The energy absorbed by plastic deformation W_{pl} is the sole difference between W_{tot} and W_{el}. Table IV gives the ratios W_{el}/W_{tot} and W_{pl}/W_{tot} as well as the maximum depth h_m and the residual depth on the film h_r which is the indentation depth at zero force. These results show as expected increases in h_m and h_r values with the maximum indentation force, and all curves exhibit an elastic–plastic deformation with a domination of the plastic deformation. The images of the residual impression of the four indentation tests can be seen in Fig. 9. The indentation depths of 1.6 and 3 μm, reached at maximum forces of 37.5 and 75 mN, are in the order of magnitude of the film roughness (rms) $R_q = 2.6$ μm. Therefore, at the first stage of the indentation, an elastic–plastic deformation occurs and this mainly happens in the Ni fibers. Furthermore, the data obtained display an increase in the elastic recovery rate with the maximum indentation force, while the plastic deformation rate shows an opposite behavior. This trend could be explained by noticing that the presence of the matrix growing with the indentation depth might deform elastically but undergo very little actual permanent deformation.

B. TP2 Mechanical Properties

In the second type of tests, 20 loading–unloading cycles were completed in order to extract the Young's modulus E and the hardness H as functions of depth. The loading of the first cycle is done with a maximum depth of 4 μm, and then the maximum depth is progressively increased by 1.4 μm for each cycle until the twentieth cycle is reached with a maximum depth of 32 μm. Each unloading step is done at the final depth equal to 40% of the maximum depth reached during the cycle. The force and the depth cycles after TP2 testing are shown in Fig. 10. The standard method of Oliver-Pharr was employed to extract E and H [15]. The evolutions of H and E as functions of indentation depth are presented in Figs. 11 and 12, respectively. The hardness and modulus are observed to have their highest values with a significant scatter when the indentation depth is less than 7 μm. This can be explained by the fact that at the first stage of the indentation, the spherical tip is in contact only with some Ni fibers of the TP2. In this case, the fibers have a great influence on the properties of the TP2 and the first term in (7) is predominant for the modulus calculation. The scattered values are related to the surface roughness of the film resulting in an inaccurate estimation of the projected area which is essential for H and E calculation. At 7-μm depth, H and E are around 0.3 and 6 GPa, respectively. Beyond 7 μm, H and E decrease as a function of depth. In fact, between 7 and 32 μm, E varies from 6 to 2 GPa, whereas H decreases from 0.3 to 0.07 GPa.

TABLE IV
DATA EXTRACTED FROM INDENTATION CURVES

F_m (mN)	h_m (μm)	h_r (μm)	$\%W_{el}/W_{\text{tot}}$	$\%W_{pl}/W_{\text{tot}}$
37.5	1.6	1.2	21.3	78.7
75	3	2.4	26.7	73.3
150	5.8	3.5	31.2	68.8

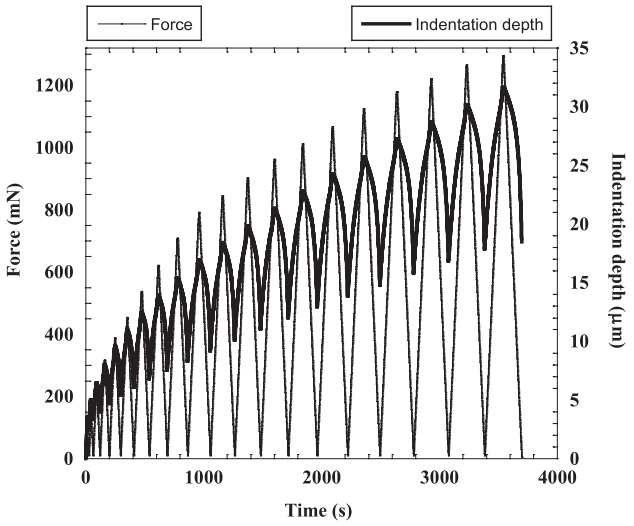

Fig. 10. Force and displacement indentation cycles.

The decrease in properties is different from homogeneous materials which usually exhibit constant H and E with the indentation depth. Here, the observed decrease with depth is due to the influence of the polyamide which has lower H and E compared to that of Ni fibers. While at the beginning of the indentation the prevalence of fibers on mechanical properties is observed, as the depth increases, the influence of fibers is reduced and the matrix takes place increasingly, hence influencing the properties. For the modulus, the expected result given in (7) is not respected because this equation takes into account neither the surface roughness nor the heterogeneous repartition of the matrix with the film thickness.

IV. ELECTRICAL AND MECHANICAL CONTACT RESULTS

A. Contact Resistance Versus Compression

The test setup shown in Fig. 6 was used to mechanically and electrically characterize the contact between dummy BGA bumps and TP2 film. Tests were performed with three bumps having diameters of 370, 470, and 650 μm, and heights of 244, 241, and 340 μm, respectively. Each curve was obtained from an average of four BGA bumps/TP2 contact tests. For all tests, the input voltage was set to 100 mV and a compliant current of 1 A was used. The first test consisted of applying onto the BGA board a uniaxial compression up to 100 μm, and the contact resistance is recorded at the same time. The contact resistance value was recorded for every 10-μm compression with a wait time between recorded points; corresponding to a test time of 200 s. The resistance evolution as a function of the amount of compression is presented in Figs. 13–15 for the bump diameters of 370, 470, and 650 μm, respectively. The second test, as presented in Fig. 16, was done with a

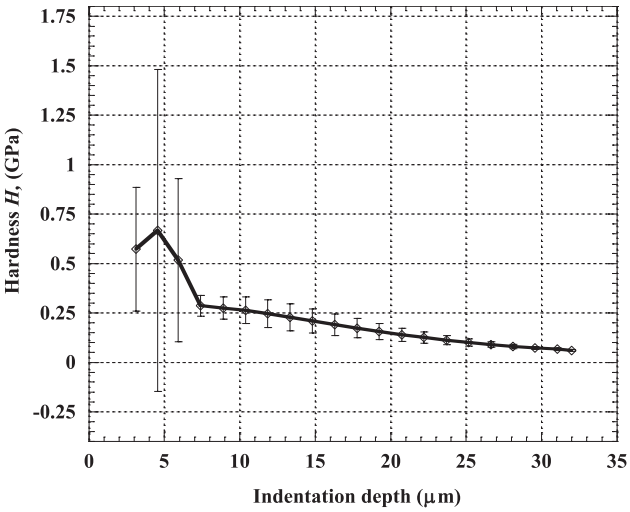

Fig. 11. Hardness as a function of indentation depth.

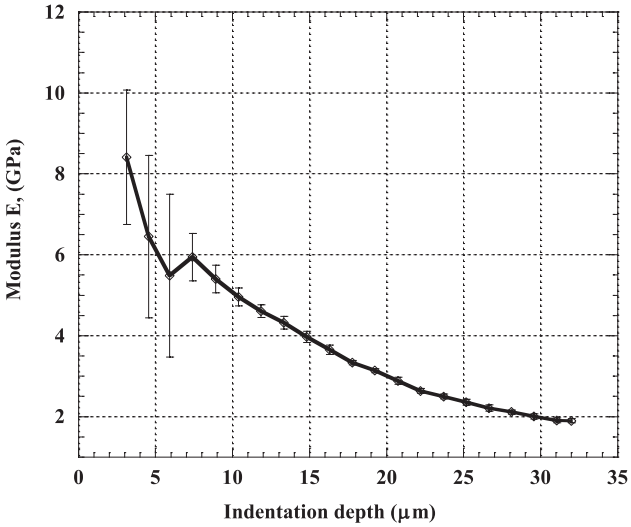

Fig. 12. Modulus as a function of indentation depth.

470-μm bump diameter by applying a compression up to 50 μm followed by a holding during 60 min. This allows studying the evolution of contact resistance with time under a holding compression condition.

The results presented in Figs. 13–15 indicate similar tendency with a progressive decrease in the contact resistance with the increase in the compression. From 80-μm compression, the contact resistance tends to a constant value of 418, 388, and 354 mΩ for the bump diameters of 370, 470, and 650 μm, respectively.

The analysis of the contact resistance evolution could be made by taking into account the geometry and the deformation mechanism of all materials involved in the contact and by considering the electrical conductive mechanism sequence seen in Fig. 17. This figure shows that the total contact resistance R_t can be calculated by accounting the following contributions.

1) The resistance of the bump R_b defined as a function of the Sn resistivity ρ_{sn} and the bump radius r_b by

$$R_b = \frac{\rho_{sn}}{2\pi . r_b}. \tag{11}$$

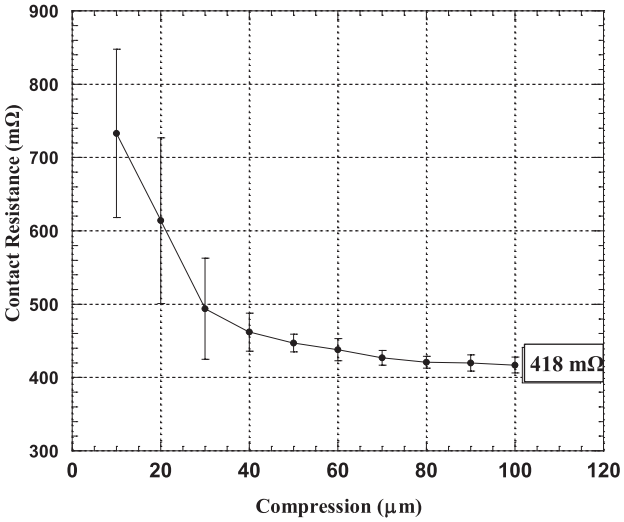

Fig. 13. Contact resistance versus compression with a 370-μm bump diameter.

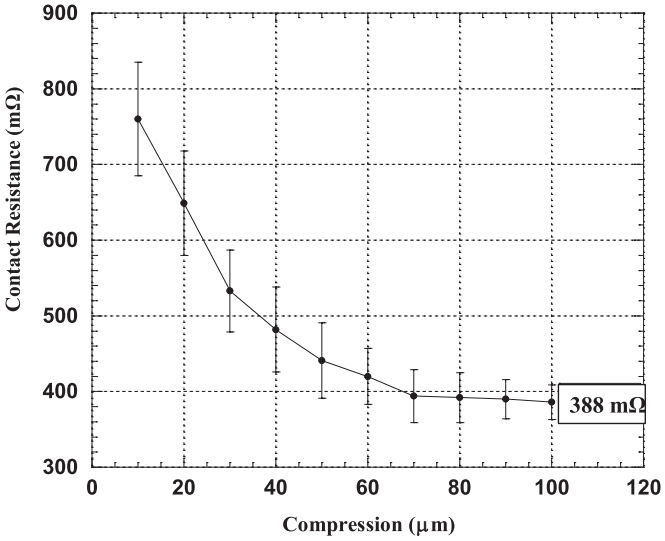

Fig. 14. Contact resistance versus compression with a 470-μm bump diameter.

By using a ρ_{sn} of 11.6 $\mu\Omega$.cm with the smallest bump diameter of 370 μm, we obtain the maximum value of R_b of 0.1 mΩ.

1) R_{Ni}, the sum of the resistances of n parallel fibers contained within the apparent contact area. R_{Ni} is expressed as function of the resistivity of the nickel material ρ_{Ni} the radius r_{Ni} and the height h_f of the fiber by

$$R_{Ni} = \frac{\rho_{Ni}.h_f}{n\pi.r_f^2}. \quad (12)$$

The average fiber pitch is 11 μm and the fiber nominal diameter is 8 μm, so that the value of n is calculated by dividing the diameter of the contact area by 11 μm. By using the diameter of the plastic deformation remained on the bump after compression (see Fig. 18) for determining n and with ρ_{Ni} of 6.84 $\mu\Omega$.cm, we obtain, for the 370-μm diameter the maximum value of R_{Ni} of 2 mΩ.

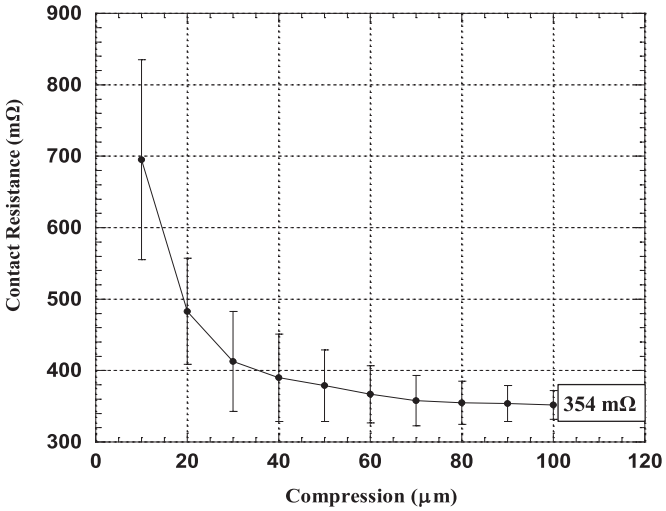

Fig. 15. Contact resistance versus compression with a 650-μm bump diameter.

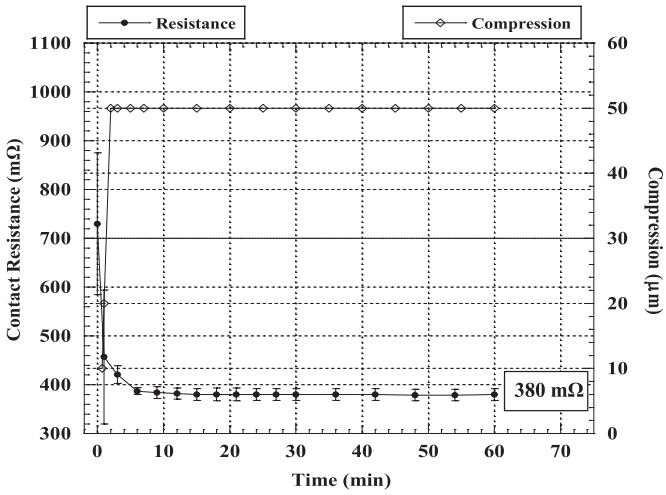

Fig. 16. Contact resistance versus time with a 470-μm bump diameter.

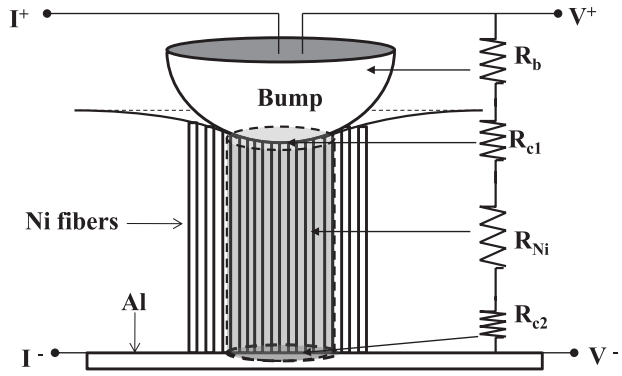

Fig. 17. Schematic of the contact resistance model.

1) The contact resistance at the interface bump/TP2 R_{c1}.
2) The contact resistance at the interface TP2/Al R_{c2}.

The calculation of the contact resistance between two bodies, such as R_{c1} and R_{c2}, was usually done by using the Holm's electric contact theory [16]. In this theory, the constriction resistance of two contacting bodies of resistivity ρ is equal

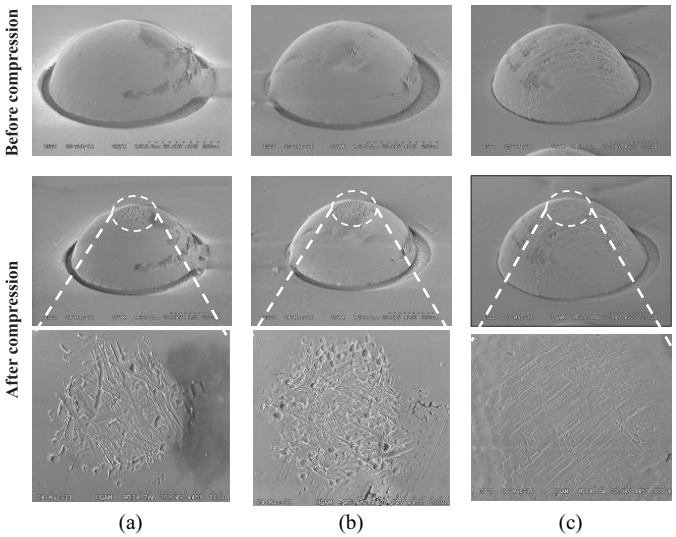

Fig. 18. SEM micrograph of bumps before and after compression. (a) 370-μm diameter. (b) 470-μm diameter. (c) 650-μm diameter.

to $\rho/2a$, where a is the radius of the contact area which is assumed to be a unique circular spot. Greenwood [17] has extended this formula to a more realistic case of multiple contact spots within the area of contact due to both the large-scale waviness and the surface roughness of the contacting materials. In the case of a large number n of circular spots situated within a single cluster, it was shown by Greenwood that the contact resistance can be approximated as

$$R_c = \frac{\rho}{2}\left(\frac{1}{nb} + \frac{1}{c}\right) \tag{13}$$

where b is the mean radius of the spots and c is the radius of the cluster.

These formulas are valid only when the contacting bodies can be considered as semi-infinite compared to the area of contact. Norberg *et al.* [18] have used numerical method to approximate the contact resistance of a thin film constituting at least one of the contacting bodies. However, we used a partially idealized model which excludes the surface roughness and the results show some uncertainties due to numerical errors. Research in [19], on the influence of the thin film on the contact resistance, was based on one contact spot and is also limited by some restriction in the film thickness and the contact area sizes. None of the above contact resistance models can be used to analyze the evolution of the resistance obtained in this paper. On the other hand, by considering the values of R_b and R_{Ni} found with (11) and (12), it is evident that the resistance values measured at the end of the compression are mainly due to the resistances at the interfaces bump/TP2 and TP2/Al. These resistances depend on the evolution of the contact area including the mode of deformation of contacting asperities. At low compression, the high and scattered resistance values could be explained by the combination of different phenomena that occur at the contacting interfaces. First, the mating components in both interfaces are metals, and so they are often covered with native oxide or electrically insulating layers. The electrical conductivity at the interface is achieved only when metal-to-metal contact occurs, that is, where insulating films are ruptured. This can be facilitated by the sharp ends of the fibers. Second, a low-compression loading corresponds to a small contact area and consequently the number of fibers electrically in contact with the bump and the Al is small leading to a low conductivity. Third, the contact between the bump and the fibers is not stable at low interfacial stresses; sliding of the fibers onto the bump can occur inducing some variations in the measured resistances. These three phenomena can explain the difference in delay between the stabilization of the resistance and the compression displacement noticed in Fig. 16. As the compression increases, the contact area expands with the number of fibers within the contact area and fibers sliding may be reduced by the increase in the interfacial stresses. As a result, the contact resistance decreases after 80-μm compression, in Figs. 13–15, the contact area experiences a little variation that may explain why the resistances tend to stable values. This stability is also found after a few minutes of holding the compression at 50 μm as shown in Fig. 16. Since the NanoPads can provide power around 100 mA, the voltage drop due to the resistances measured here is less than 50 mV which is low enough to meet the electrical requirements of the WaferBoard WLP application.

B. Materials Failure Analysis

After compression, the characterization of the solder bumps, the Al film, and both sides of the TP2 film were performed. Fig. 18 shows the SEM micrographs of the bumps before and after 100-μm compression. For all the three bump diameters, a residual plastic impression is shown on the bumps after compression. The residual plastic impression displays a penetration of the Ni fibers into the bump material combined with an anisotropic sliding. This may result from elastic or elastic–plastic buckling of the fibers under compressive stress. It is clear that this behavior does not corroborate the Rosen's extension and shear buckling models reported in Section II-B. These models consider the fibers as an infinite array of regularly spaced and parallel plates embedded in elastic matrix. Unlike this, the actual TP2 film is intentionally made with fibers 5° tilted and 3 μm spaced but with some spacing imperfections. Under compressive loading, this fiber configuration allows the fibers to bend in different directions depending on the matrix density around each fiber as seen in Fig. 18. However, the sliding of some Ni fibers is not so critical since the contact resistance tends toward a stable value and no plastic damage was seen after the SEM inspection of the TP2 top surface. The diameters of the residual plastic impressions are 140, 168, and 195 μm for the bump diameters of 370, 470, and 650 μm, respectively. Thus, we noticed an increase in the plastic contact area when the bump diameter increases. This explains, as displayed in Figs. 13–15, the decrease in the final resistance values measured at 100-μm compression.

The characterization of the Al film and both sides of the TP2 film indicates that no residual impression was seen on the surface materials. Hence, the deformation of the Al and TP2 films can be considered as purely elastic. However, some traces of Sn from the solder bumps were found onto the top side of the TP2 film. Fig. 19 is an SEM micrograph of the TP2

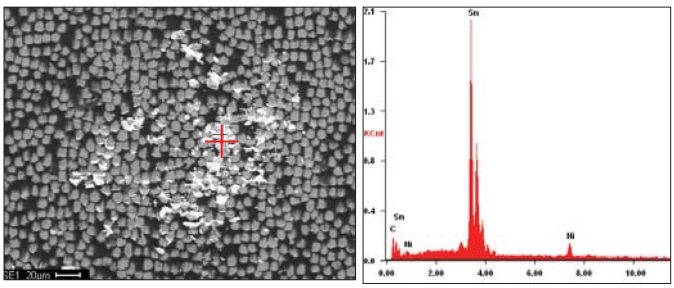

Fig. 19. SEM micrograph of the contact area on TP2 surface with the EDX spectra showing Sn traces.

contact area and its correspondent EDX spectrum confirming the presence of a large Sn peak. The elastic regime occurs on the TP2 and Al films because the mean contact pressure at the interfaces bump/TP2 and TP2/Al may be, respectively, lower than the yield strength of the TP2 and the Al. Instead, the mean contact pressure at the interface bump/TP2 may be higher than the yield strength of the Sn material, so a plastic flow exists in the bump. These explanations can be correlated by means of the hardness since the yield strength which represents the transition between elastic and plastic regimes is known to increase with the hardness [20]. Indeed, the Sn hardness which varies between 0.045 and 0.060 GPa [21] is lower than the TP2 hardness measured by indentation in Fig. 11. Besides, Ni has bulk hardness between 0.8 and 1.8 GPa [21]; these values combined with the pointed ends of the fibers can easily explain the penetration of the Ni fibers into the Sn bump during the compression. The elastic deformation of the Al film after compression can be explained by the fact that the hardness of the Al film of around 0.6 GPa [22] is greater than the hardness of the TP2 measured in Fig. 11. The sliding observed on the bump contact area could mean that the fibers undergo a small amount of reversible buckling in all directions.

V. Conclusion

A study of ACF based on vertical fibers was presented in this paper for use in the WaferBoard platform. The chosen ACF, called TP2, meets the requirements of WLP application presented in this paper in terms of size and high-density interconnection. For the mechanical properties, indentation tests showed that the elasticity of the TP2 increases with indentation depth while the plasticity decreases. This behavior was due to the predominance of the Ni fibers at the top surface of the TP2 while the influence of the polyamide matrix increases with indentation depth. For the same reasons, the measured Young's modulus and the hardness decreased with the indentation depth.

For WLP applications, dummy BGA boards were manufactured and tested in compression contact with the TP2 deposited onto the Al film. This stack allows evaluating the efficiency of the electrical contact of the TP2 film for a WLP application. Without any bonding or laminating of the TP2, we observed a decrease in the resistance with the compression, and low and stable resistance values less than 500 mΩ were obtained after 80 μm of compression. Stable resistance values were also seen after few minutes of holding the compression at 50 μm. SEM characterization showed that a plastic deformation occurred in the bump solder, and the Ni fibers of the TP2 were shown to penetrate into the bump with an anisotropic sliding. This behavior is primordial for the establishment of the electrical contact. The samples' deformation could be explained by the mean contact pressure and the hardness of the materials in contact. The TP2 and Al film exhibit elastic deformation. This result is very encouraging for the use of nonpermanent bonding ACF in WLP applications.

Some additional experiments need to be addressed before a wide adoption of ACF-based vertical fibers. These studies must include moisture absorption, creep phenomenon, fatigue cycling, and heating effect analysis due to both high current values through the ACF and heat losses from the circuitry.

Acknowledgment

The authors would like to thank all the ACF companies presented in this paper for providing samples, as well as J. Browne from Btechcorp for the technical discussions and the close collaboration. They would also like to thank J. Chevalier for the mechanical press manufacturing.

References

[1] K.-W. Jang and K.-W. Paik, "Effects of anisotropic conductive film viscosity on ACF fillet formation and chip-on-board packages," *IEEE Trans. Electron. Packag. Manufact.*, vol. 32, no. 2, pp. 74–80, Apr. 2009.

[2] H.-Y. Son, C.-K. Chung, M.-J. Yim, and K.-W. Paik, "Wafer level package using pre-applied anisotropic conductive films (ACFs) for flip-chip interconnections," in *Proc. 56th IEEE Electron. Compon. Technol. Conf.*, 2008, pp. 565–569.

[3] S. H. Fan and Y. C. Chan, "Effect of misalignment on electrical characteristics of acf joints for flip-chip on flex applications," *Microelectron. Rel.*, vol. 42, no. 7, pp. 1081–1090, 2002.

[4] L. K. Teh, M. Teo, E. Anto, C. C. Wong, S. G. Mhaisalkar, P. S. Teo, and E. H. Wong, "Moisture-induced failures of adhesive flip-chip interconnects," *IEEE Trans. Compon. Packag. Technol.*, vol. 28, no. 3, pp. 506–516, Sep. 2005.

[5] R. S. Norman, "Reprogrammable circuit board with alignment-insensitive support for multiple component contact types," U.S. Patent 11 611 263, Dec. 15, 2006.

[6] M. D. Diop, M. Radji, W. Andre, Y. Blaquiére, A. A. Hamoui, and R. Izquierdo, "Electrical characterization of annular through silicon vias for a reconfigurable wafer-sized circuit board," in *Proc. 19th IEEE Electr. Perform. Electron. Packag. Syst.*, Austin, TX, USA, Oct. 2010, pp. 245–248.

[7] T. Ikeda, W. K. Kim, and N. Miyazaki "Evaluation of the delamination in a flip-chip using anisotropic conductive adhesive films under moisture/reflow sensitivity test," *IEEE Trans. Compon. Packag. Technol.*, vol. 29, no. 3, pp. 551–559, Sep. 2006.

[8] D. Gay, *Materiaux Composites*, 4th ed. Paris, France: Hermes, 1997, pp. 55–73.

[9] S. W. Tsai, "Structural behavior of composite materials," NASA, Washington, DC, USA, Tech. Rep. CR-711964, 1965.

[10] R. Jones, *Mechanics of Composite Material*, 2nd ed, Neywork, USA: Taylor & Francis, 1999, p. 172.

[11] B. W. Rosen, "Mechanics of composite strengthening," *Fiber Composite Materials*, Metals Park, OH, USA: ASM, 1965, pp. 37–75.

[12] I. Yeo, C. C. Liu, and E. J. Kim, "Predictive dynamic thermal management for multicore systems," in *Proc. 45th ACM/IEEE Design Autom. Conf.*, Jun. 2008, pp. 734–739.

[13] J. E. Jakes, J. C. Hermanson, and D. S. Stone, "Nanoindentation of the interphase region of a wood-reinforced polypropylene composite," in *Proc. 9th Int. Conf. Wood Biofiber Plastic Composites*, May 2007, pp. 197–203.

[14] S. H. Lee, S. Wang, G. M. Pharr, and H. Xu, "Evaluation of interphase properties in a cellulose fiber-reinforced polypropylene composite by Nanoindentation and finite element analysis," *Composites, A, Appl. Sci. Manuf.*, vol. 38, no. 6, pp. 1517–1524, Jun. 2007.

[15] W. C. Oliver and G. M. Pharr, "An improved technique for determining hardness and elastic modulus using load and displacement sensing indentation experiments," *J. Mater. Res.*, vol. 7, no. 6, pp. 1564–1583, 1992.
[16] R. Holm, *Electrical Contacts, Theory and Applications.*, 4th ed. Berlin, Germany: Springer-Verlag, 1967.
[17] J. A. Greenwood, "Constriction resistance and the real area of contact," *Brit. J. Appl. Phys.*, vol. 17, no. 12, p. 1621, 1966.
[18] G. Norberg, S. Dejanovic, and H. Hesselbom, "Contact resistance of thin metal film contacts," *IEEE Trans. Compon. Packag. Technol.*, vol. 29, no. 2, pp. 371–378, Jun. 2006.
[19] R. S. Timsit, "Constriction resistance of thin film contacts," *IEEE Trans. Compon. Packag. Technol.*, vol. 33, no. 3, pp. 636–642, Sep. 2010.
[20] A. C. Fischer-Cripps, *Nanoindentation, Mechanical Engineering Series*, 2nd ed. New York, USA: Springer-Verlag, 2004, p. 9.
[21] P. G. Slade, *Electrical Contact: Principles and Applications*, 1st ed. New-York, USA: CRC Press, 1999, p. 1024.
[22] R. Saha and W. D. Nix, "Effects of the substrate on the determination of thin film mechanical properties by Nanoindentation," *Acta Mater.*, vol. 50, no. 1, pp. 23–38, 2002.

Mamadou Diobet Diop (M'11) was born in Tivaouane, Senegal. He received the M.Eng. degree in engineering physics from the Centre Universitaire des Sciences et Techniques, Université Blaise Pascal, Clermont-Ferrand, France, in 2005, and the Ph.D. degree in microelectronics from the Ecole Nationale Supérieure des Mines de Saint-Etienne, Saint-Etienne, France, in 2009.

He has been a Post-Doctoral Fellow with the Université du Québec à Montréal, Montreal, QC, Canada, since 2009, in a rapid prototyping platform for electronic systems. His role focuses on the electrical testing and the thermal management of through silicon vias as well as the characterization of anisotropic conductive adhesive for WLP application. He is currently a Post-Doctoral Fellow with Université de Sherbrooke, Sherbrooke, U.K., and he works for IBM Bromont on flip chip on package reliability issues. His current research interests include mechanical and electrical tests of thin films, 3-D interconnects, and packaging for system in package.

Moufid Radji (SM'09) was born in Porto-Novo, Benin. He received the B.Eng. (Hons.) and M.Eng. degrees in electrical engineering from McGill University, Montreal, QC, Canada, in 2008 and 2010, respectively, and the Graduate Certificate in management with a concentration in treasury and finance from the Institution's School of Continuing Studies in 2010.

He is focused on wafer-level packaging techniques to develop 3-D-ICs. He has served multiple terms as a Teaching Assistant on signal processing, microelectronics laboratory, and microfabrication courses. His current research interests include silicon wafer post-processing, large area integrated circuits, interconnects, and signal integrity.

Anas A. Hamoui received the B.Eng. (Hons.) degree from Kuwait University, Kuwait, in 1996, the M.Eng. degree from McGill University, Montreal, QC, Canada, in 1998, and the Ph.D. degree from the University of Toronto, Toronto, ON, Canada, in 2004.

He was a Research Assistant with the Microelectronics and Computer Systems Laboratory, McGill University, from 1996 to 1998, working in the area of timing and power analysis of submicron CMOS digital circuits. From 1998 to 2004, he was a Research Assistant and a part-time Instructor with the Electronics Group, University of Toronto, working in the area of analog and mixed-signal integrated circuits (ICs) for high-speed data communications. Since 2004, he has been an Assistant Professor with the Department of Electrical and Computer Engineering, McGill University. His current research interests include analog and mixed-signal ICs for wireless communications and biomedical applications.

Dr. Hamoui is an Associate Editor of the IEEE TRANSACTIONS ON BIOMEDICAL CIRCUITS AND SYSTEMS and Associate Editor of the IEEE TRANSACTIONS ON CIRCUITS AND SYSTEMS I: REGULAR PAPERS. He was Co-Guest Editor of the 2010 Special Issue of the IEEE TRANSACTIONS ON BIOMEDICAL CIRCUITS AND SYSTEMS with selected papers from the 2010 IEEE International Solid-State Circuits Conference (ISSCC). He was Co-Chair of the Technical Program Committee for the 2009 IEEE International Conference on Electronics, Circuits, and Systems, the flagship conference of the IEEE Circuits and Systems Society in IEEE region 8. He is co-Chair of the Montreal Chapter of the IEEE Solid-State Circuits Society, the recipient of the 2007 Outstanding Chapter Award. He received the Professor of the Year Award by the Electrical, Computer, and Software Engineering Student Society (for two consecutive years) for his teaching of microelectronic circuits to undergraduate students. His contributions to the teaching of microelectronic circuits also comprise writing the SPICE sections (including device models, circuit macromodels, and design examples) at the end of each chapter in the widely-utilized textbook Microelectronic Circuits by A. S. Sedra and K. C. Smith.

Yves Blaquière (M'86) received the B.Ing., M.Sc.A, and Ph.D. degrees in electrical engineering from École Polytechnique de Montréal, Montréal, QC, Canada, in 1984, 1986, and 1992, respectively.

He has been a Professor with Université du Québec à Montréal (UQAM), Montréal, since 1987. He works in the field of electrical/electronic/microelectronic engineering, specifically in ASIC/FPGA design, VLSI/WSI microsystems, high speed digital circuits, timing tools, architectures, defect tolerance and applications to signal processing, network/high speed processors, and switches. He has been involved in research and development projects in collaboration with several microelectronic companies, such as Gestion TechnoCap Inc., DreamWafer Division, Hyperchip Inc. In particular, he was involved in WSI research with Hyperchip Inc., from 1997 to 2004, including a two year period where he contributed full time as a Technical Lead Researcher and a Manager of a team of 35 ASIC/FPGA engineers, to deliver a core internet protocol petabit router. He also collaborates in research with several professors from other universities, especially with Université du Québec à Montréal, École Polytechnique Montréal, École de Technologie Supérieure de Montréal, Universités du Québec en Outaouais, and Université du Québec à Chicoutimi. He was the Director of Laboratoire de Recherche de Conception en Microélectronique, UQAM, from 1992 to 1999 and 2004 to 2008, the Director of the microelectronic engineering program from 2004 to 2010 at UQAM, and the Director of engineering at UQAM.

Prof. Blaquière is a member of the Ordre des Ingénieurs du Québec.

Ricardo Izquierdo (M'06) received the Ph.D. degree in engineering physics from École Polytechnique de Montréal, Montréal, QC, Canada, in 1998.

He joined the Microelectronics Engineering Program with the Computer Science Department, Université du Québec à Montréal, Montréal, in July 2005, after seven years in the industry as a Researcher then the Director of R&D with the Technologies Novimage and OLA Display Corporation. He contributed to the emergence of a nucleus of research activity in the field of organic electronics in the Montreal area. He is the Director of the Co-design and Fabrication of Microsystems Research Center. He has significant experience in the deposition and characterization of electroactive materials as well as in micro- and nanofabrication technologies and the development of micro-devices (e.g., MEMS, OLEDs, and sensors).